crystals

MDPI

Article

Fe_2O_3-Ag_2O/TiO_2 Nanocatalyst-Assisted LC-MS/MS-Based Detoxification of Pesticide Residues in *Daphnia magna* and Algae Mediums

Faheem Ahmed [1,*], Tentu Nageswara Rao [2], Nishat Arshi [3], Y. Prashanthi [4], Shalendra Kumar [1,5] and Adil Alshoaibi [1]

[1] Department of Physics, College of Science, King Faisal University, P.O. Box-400, Al-Ahsa 31982, Saudi Arabia; sjagdish@kfu.edu.sa (S.K.); adshoaibi@kfu.edu.sa (A.A.)
[2] Department of Chemistry, Krishna University, Machilipatnam 521004, India; tnraochemistry@gmail.com
[3] Department of Basic Sciences, Preparatory Year Deanship, King Faisal University, P.O. Box-400, Al-Ahsa 31982, Saudi Arabia; nshastri@kfu.edu.sa
[4] Department of Chemistry, Mahatma Gandhi University, Nalgonda 508001, India; puttaprashanthi@gmail.com
[5] Department of Physics, School of Engineering, University of Petroleum & Energy Studies, Dehradun 248007, India
* Correspondence: fahmed@kfu.edu.sa

Abstract: In this work, a simple sensitive validated liquid chromatography mass spectroscopy (LC-MS/MS) analytical method was developed for the determination of Spirodiclofen residues in different aquatic toxic media. The toxic media were those that provide nutrients and help with the growth of different aquatic organisms for their survival and multiplication. The different media were the M4 medium for *Daphnia magna* and The Organization for Economic Cooperation and Development (OECD TG 201) medium for alga. Fe_2O_3-Ag_2O/TiO_2 nanocomposites were prepared by using a precipitation method, which was used as a photo-catalyst for the removal of Spirodiclofen pesticide from aquatic media. The experiment was performed under direct sunlight at a single fortification level (1.0 µg/mL) in M4 and OECD TG 201 media. The optimum catalyst concentration for the complete degradation was found to be 10 mg/L under sunlight. Spirodiclofen residues in water were determined by LC-MS/MS, and the rate constant DT50 (half-life) values were calculated from the obtained data. The results showed that with Fe_2O_3-Ag_2O/TiO_2 nanocatalyst, the DT50 (half-life) value was found to be approximately 8 h. These results revealed that iron-oxide- and silver-oxide-incorporated TiO_2 nanocomposites were excellent photocatalysts when compared with TiO_2, Fe_2O_3-TiO_2, and Ag_2O-TiO_2 for the decontamination of pesticide residues in aquatic media samples.

Keywords: TiO_2 nanocomposites; aquatic media; Spirodiclofen; XRD; SEM; LC-MS/MS; DT50

Citation: Ahmed, F.; Rao, T.N.; Arshi, N.; Prashanthi, Y.; Kumar, S.; Alshoaibi, A. Fe_2O_3-Ag_2O/TiO_2 Nanocatalyst-Assisted LC-MS/MS-Based Detoxification of Pesticide Residues in *Daphnia magna* and Algae Mediums. *Crystals* **2023**, *13*, 644. https://doi.org/10.3390/cryst13040644

Academic Editors: Assem Barakat, Saied M. Soliman and Ayman El-Faham

Received: 1 February 2023
Revised: 5 April 2023
Accepted: 7 April 2023
Published: 9 April 2023

1. Introduction

Ecotoxicology is markedly different from environmental toxicology in that it involves the effects of stressors at all levels of biological organization, from the molecular level to entire communities and ecosystems [1–3]. The study of ecotoxicology is a multi-step process that includes the entry, distribution, and fate of pollutants in the environment; the entry and fate of pollutants in living (biota) organisms within an ecosystem; and the harmful effects of chemical pollutants on the ecosystem constituents [4].

Pesticide contamination of the environment is a serious environmental concern because these compounds can harm human and ecosystem health [5–7]. A significant amount of pesticides that are applied enter the soil, sediments, and water, where they can undergo various transformation processes that can result in the formation of stable transformation products in aquatic environments [7–10]. The toxicity of various transformation processes may significantly differ from that of the parent compound [11,12]. Pesticides are widely used in agricultural practices. Pesticides have the potential to harm nontarget organisms

such as algae. As a result, their potential effects on aquatic primary producers are critical and must be investigated through ecotoxicological experiments [13]. Light, temperature, and pH are important environmental parameters that can affect alga population growth and the behavior of organic contaminants in aquatic systems [14–16]. *Pseudokirchneriella subcapitata* is a nonmotile unicellular green alga found in most freshwater environments. Additionally, *Chlorococcum* sp. is a green alga found on land (*Chlorophycea*). These organisms are critical to the maintenance of ecological balance in both aquatic and terrestrial environments. As a result, any interaction of pesticide contaminants with algae and their activities could harm ecosystem health [17–19].

Herbicides have the potential to alter the structure and function of aquatic populations by changing the species composition of an alga community [20]. Pesticides are beneficial to agriculture, but they frequently enter aquatic environments after spraying or rainfall, affecting nontarget organisms, disrupting the food chain, altering the food web, and causing an imbalance in the entire ecosystem [21]. The Organization for Economic Co-operation and Development (OECD) has specified bioassays using alga, daphnia, and fish to estimate the likely effects of various substances on aquatic ecosystems. Algae are the primary producers in aquatic ecosystems, according to this guideline [22]. Alga populations are used to determine the toxicity of wastes and to receive water. For a wide range of chemicals, algae growth inhibition tests are relatively sensitive bioassays.

Herbicides are expected to be more toxic to algae than to other aquatic organisms because the compounds' targets are usually either photosynthesis or energy transport enzymes [23,24]. To understand the complete photolysis of pesticides and their breakdown products, as well as to ensure that water is clean and safe, biological indicators such as algae are used.

Spirodiclofen may be a carcinogenic pesticide to humans, according to the United States Environmental Protection Bureau14 [25,26]. Spiromesifen causes skin sensitization. Spiromesifen-alcohol is the primary metabolite of Spirodiclofen [27–29]. Pesticides can pollute the soil, water, and air, producing acute and chronic toxicity effects. Consuming contaminated food causes nonbiodegradable pesticides to bioaccumulate in the human body, resulting in chronic illness and indirect effects such as birth defects, genetic modification, nervous disorders, cancers, and reproductive diseases. Because of its simplicity and sustainability, photocatalysis is the most advanced and appropriate technique for pesticide treatment. Metal oxide semiconductors function as heterogeneous photocatalysts for the removal of organic contaminants such as oxides of phosphorus (Cu, Mn, Co, Cr, V, Ti, Bi, and Zn). Zinc oxide (ZnO) and titanium oxides (TiO_2) are photoactive with high incident photoelectric conversion efficiency, are chemically stable, have high photostability, and are resistant to corrosion over long periods [30,31].

Because of its remarkable photodegradation activity, superior physicochemical properties, nontoxic nature, and low cost, TiO_2 is one of the semiconductor materials often used in photocatalysis. However, the photocatalytic properties of TiO_2 are weakened under direct solar irradiation and are limited to UV light, which might be due to the wide bandgap energy (3.0–3.2 eV) and high electron–hole (e^-/h^+) recombination rate [32]. Thus, to improve the photocatalytic properties of TiO_2 and reduce these problems, various efforts, including doping of heterojunctions with equivalent and/or different bandgap materials and chemical surface modifications, have been made [33–39]. Furthermore, for doping and bandgap tuning of TiO_2, hematite (α-Fe_2O_3) was found to be a suitable material owing to its narrow optical bandgap (~2 eV), outstanding chemical strength, as well as wide availability in nature. Doping of α-Fe_2O_3 in TiO_2 could help in promoting the absorption of photons with lower energy, finally resulting in enhanced photocatalytic efficiency [34–39]. On the other hand, Ag_2O, as an excellent photosensitizer with a low bandgap energy (1.2 eV), can be combined with Fe_2O_3 and TiO_2 to prevent photodecomposition of pure Ag_2O. Therefore, TiO_2 incorporated with Fe_2O_3 and Ag_2O can reduce charge recombination and enhance photocatalytic performance [40,41].

To assess the aforementioned issues, in this work, we aimed to determine the photocatalytic activity of Spirodiclofen pesticide residues using Fe_2O_3-Ag_2O/TiO_2 in aquatic media exposed to direct sunlight. The LC-MS/MS method was used to confirm the residues. Experiments were also carried out to assess the growth of green alga and daphnia in water in the presence of pesticide residues.

2. Experimental details

2.1. Materials and Methods

Reference Standard, Reagents, and Solutions

The Spirodiclofen reference standard (purity 99.1%) was obtained from Sigma Aldrich (Bangalore, India). The formic acid, Acetonitrile and water used were MS-grade. $NaHCO_3$, NH_4Cl, $MgCl_2.6H_2O$, $CaCl_2.2H_2O$, $MgSO_4.7H_2O$, KH_2PO_4, $FeCl_3.6H_2O$, $Na_2EDTA.2H_2O$, H_3BO_3, $MnCl_2.4H_2O$, $ZnCl_2$, $CoCl_2.6H_2O$, $Na_2MoO_4.2H_2O$, $CuCl_2.2H_2O$, ethanol, ammonium hydroxide, silver nitrate, tetra butyl ortho titanate, ferric nitrate, and isopropyl alcohol were purchased from Merck India Pvt Ltd. (Bangalore, India). and Milli-Q water was obtained from Millipore India Ltd., Bangalore, India.

2.2. Preparation of Iron-Oxide- and Silver-Oxide-Incorporated TiO_2

In a typical synthesis, 1.0 mmol of ferric nitrate was ultrasonically dispersed in anhydrous ethanol for 1 h (40 mL). This solution was diluted with 4.5 mL of concentrated ammonium hydroxide, and, to this solution, 1.0 mmol of silver nitrate was quickly added under vigorous stirring. The solution was stirred for 12 h, and the product was washed three times with anhydrous ethanol. The final product was placed in anhydrous ethanol (40 mL). Following that, 20 mmol of tetrabutyl ortho-titanate (TBOT) (5.0 mL) dissolved in isopropyl alcohol (40.0 mL) was dropped into the system, followed by heating the solution to ~70 °C. The entire solution was vigorously stirred for 12 h, after which the red-brown precipitates were washed several times with deionized water and ethanol, and dried in a vacuum oven at 80 °C for 24 h. Finally, the products were calcined in air at 200 °C for 2 h. To prepare a pure TiO_2 sample, the above-mentioned procedure was adopted without the addition of ferric nitrate and silver nitrate.

2.3. Characterization

The samples' structural properties were determined using an X-ray diffractometer (Philips X'Pert; MPD 3040, EA Almelo, The Netherlands) equipped with CuKα radiation in the 2θ-range of 10–80°. The crystal structure and phase purity of the sample were studied, and the crystallite size was determined using the Debye–Scherrer equation from the XRD patterns. SEM (TESCAN, CZ/MIRA I LMH) was used to examine the surface morphology of nanocomposites. TEM was used to investigate particle size and shape (FEI, TECNAI G2 TF20-ST; Oregon, USA). The infrared transform (FT-IR) spectra of KBr pellets were recorded using a JASCO FT/IR-6300 (Easton, MD 21601, USA) FT-IR spectrometer. The specific surface area was measured by nitrogen adsorption/desorption using a Micromeritics ASAP 2020 (Norcross, GA 30093, USA) instrument.

2.4. LC-MS/MS Chromatographic Conditions

A Shimadzu LC-MS/MS-8050 Infinity series LC system consisting of a binary pump, an auto sampler, a thermostat, and a mass detector was connected to triple quad LC/MS-MS spectrometer equipped with a Jet Stream technology ion source. The chromatographic separation was performed on a Phenomenex-C18 (150 mm × 4 mm, 3.5 µm). The mobile phase consisted of 0.1% formic acid in water 20% (A) and 0.1% formic acid in acetonitrile 80% (B). The flow rate was 1.0 mL min^{-1}, and the injection volume was 10 µL. The electrospray ionization source was operated in positive ion mode. The operating parameters were as follows: heat block temperature was 450 °C, desolvation temperature was 140 °C, gas flow was 15 L min^{-1}, drying gas flow was 10 L min^{-1}, and nebulizer gas flow was 4 L min^{-1}. Ion acquisition was performed in the multiple reaction monitoring (MRM) mode.

The LC-MS/MS transition for quantification and confirmation as well as the optimized multiple reaction used a quantifier of 411.10 > 71.20 *m/z*. In multiple reaction monitoring (MRM), 411.10 was the parent ion, and 71.20 was the daughter ion.

2.5. Effect of Catalyst Amount

To investigate the effect of the amount of Fe_2O_3-Ag_2O/TiO_2 nanocatalyst on the decontamination of pesticide in media, the media were spiked with 1 mL of 1000 mg/L stock solution of pesticide formulation to produce a 1 mg/L concentration of pesticide active in the media. We loaded the Fe_2O_3-Ag_2O/TiO_2 nanocatalyst by varying the concentration (1, 5, 10, 15, and 20 mg/L) in the media (separate one-liter glass bottle was maintained for each amount of Fe_2O_3-Ag_2O/TiO_2). Before being exposed to sunlight, the samples were sonicated in the dark for 10 min to achieve an even dispersion of the Fe_2O_3-Ag_2O/TiO_2 nanocomposites in water and adsorption equilibrium. In February, the bottles were exposed to sunlight from 8 a.m. to 5 p.m. Three replicates were performed.

2.6. Photocatalytic Studies

Photocatalytic experiments were conducted in a borosilicate glass bottle outside in the sunlight. To obtain 1 ppb of active pesticide concentration, 1 mL of a 1000 ppb stock solution of the pesticide formulation was added to each liter of the alga and daphnia solution. The resulting suspension was sonicated in the dark for 10 min before exposure to the sun to achieve adsorption equilibrium and obtain an even dispersion of TiO_2, Fe_2O_3-TiO_2, Ag_2O-TiO_2, and Fe_2O_3-Ag_2O/TiO_2 nanocomposites. The samples were then placed under sunlight, and the schematic representation of the photocatalysis reaction is shown in Figure 1. Samples were taken in aliquots at predetermined intervals. Media samples were taken during that time at a temperature of 27 °C. The samples were filtered using a 0.2 m PTFE membrane filter, and the filtrates were collected into vials that were amber in color. Before LC-MS/MS analysis, all the samples were kept in the dark at 5 °C. A Beckman cooling centrifuge was used to centrifuge the samples that had been enhanced with nanoparticles at 4000 rpm for 10 min at 5 °C. To prevent further residue degradation, the supernatant was transferred into amber-colored bottles and kept there until analysis in the dark at a temperature of 5 °C. The residue levels were estimated over time using the first-order kinetic equation. The pseudo-first-order kinetics take the form of

$$ln\left(\frac{C_t}{C_0}\right) = k\,t$$

$$t_{1/2} = DT_{50} = \frac{ln2}{k}$$

$$k = \frac{2.303}{t} \times \log_{10}\left(\frac{C_0}{C_t}\right)$$

where C_0 is the Spirodiclofen concentration at time zero; C_t is the Spirodiclofen concentration at time *t; k* is the rate constant; DT50 is the half-life.

2.7. Sampling

Test samples were taken from the bottle at various depths and intervals following exposure to sunlight (0, 3, 8, 16, 24, and 48 h for the photocatalytic experiment). The samples were collected, centrifuged, filtered through a 0.2 µm filter, and then analyzed using LC-MS/MS.

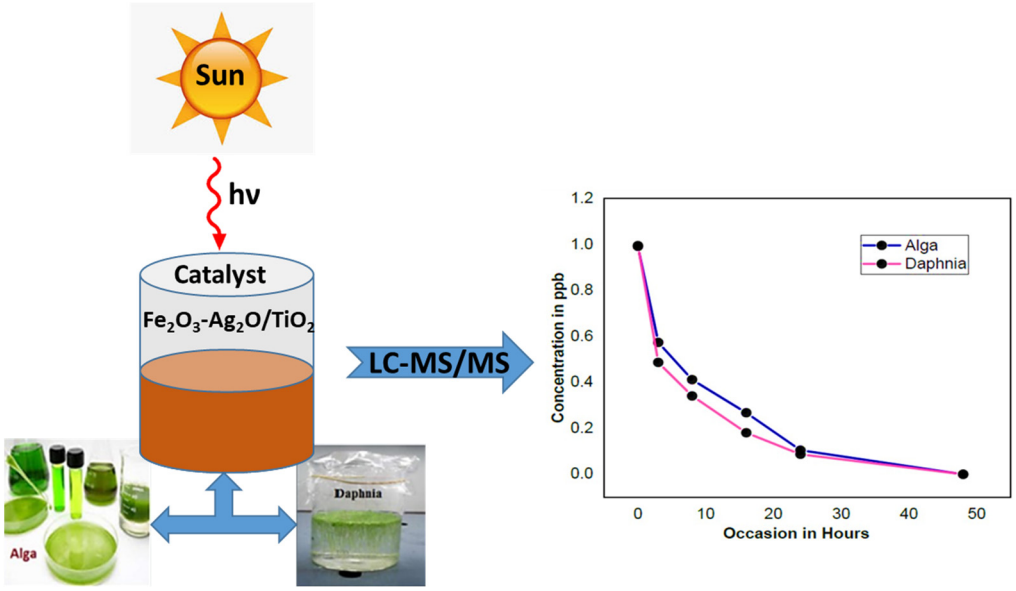

Figure 1. Schematic diagram of photocatalysis.

3. Results and Discussion

3.1. Method Validation

Specificity

We found no interference from the injections of mobile phases (0.1 % formic acid in water (20%) and 0.1 % formic acid in acetonitrile (80%)), control, or blank contributing to more than 30% of the peak area of Spirodiclofen. The longer retention times of Spirodiclofen in the injections of the test or reference item solutions were found to be comparable (Table 1). This indicated the specificity of the analysis to Spirodiclofen in alga and daphnia.

Table 1. Specificity results.

Sample ID	Intensity	Retention Time (min)
Control (Alga and Daphnia)	BDL	BDL
Mobile Phase A	BDL	BDL
Mobile Phase B	BDL	BDL
Reference Standard	45,064	5.231
Test item	44,859	5.230

3.2. Below Detectible Limit (BDL)

Linearity Data and Curve of Reference Standard

The plot of area vs. respective concentration produced a linear regression curve (Figure 2) with a correlation coefficient of −0.9996, an intercept of 6462.28, and a slope of 42,098.73. Therefore, the response from 0.1 ppb to 25 ppb was found to be linear and the following acceptance criterion was met: the correlation coefficient was greater than 0.99.

3.3. Assay Accuracy and Precision in Alga and Daphnia magna

Multiple recovery control samples (n = 5) at each of two fortification levels equivalent to 0.5 ppb and 5 ppb for both the alga and *Daphnia magna* media were collected. Additionally, Spirodiclofen in the final solution was assayed using LC-MS/MS.

For the alga and *Daphnia magna*, the overall assay accuracies of the 95.49% and 94.45% recoveries, respectively, and the precision relative standard deviation (RSD) of 1.24% and 0.58%, respectively, indicated an acceptable analysis method for the low-level concentration. The overall assay accuracies of the 98.34% and 98.71%, respectively, recoveries and precision relative standard deviation (RSD) of 0.47% and 0.57%, respectively, indicated an

acceptable method of analysis for the high-level concentration. The results are presented in Tables S3 and S4.

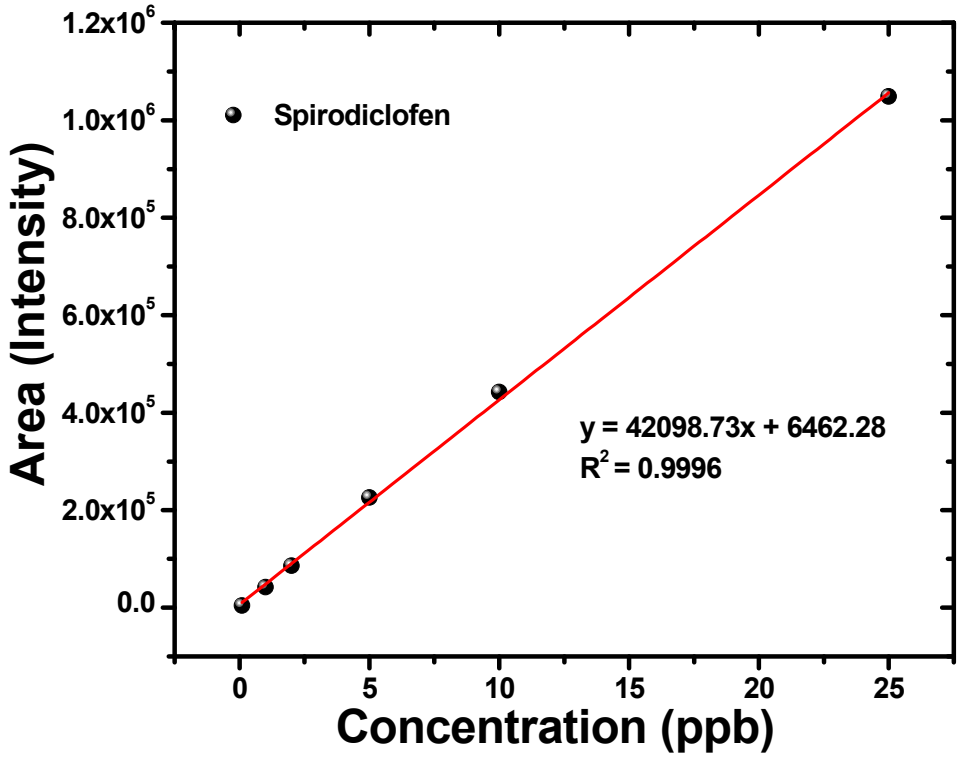

Figure 2. Linear regression curve of Spirodiclofen.

3.4. Characterizations of Nanocatalyst

3.4.1. XRD Analysis

Figure 3 illustrates the XRD patterns of pure TiO_2 and Fe_2O_3-Ag_2O/TiO_2 nanocomposites. For pure TiO_2, well-defined diffraction peaks were located at 25°, 38°, 48°, 54°, 62°, 68°, and 74° and were assigned to the crystal planes (101), (004), (200), (211), (116), (220), and (215), respectively. This XRD characteristic pattern is consistent with the standard JCPDS values of anatase TiO_2 with a tetragonal structure (JCPDS Card No. 21-1272), which did not appear in rutile or brookite form. The XRD pattern of nanocomposites showed all of the peaks of TiO_2 in addition to the lower-intensity peaks corresponding to Fe_2O3 and Ag_2O. It was observed that the diffraction peaks of 2θ for Ag_2O were positioned at angles of 37.82°, 54.31°, and 78.00° which correspond to (200), (220), and (311), respectively. These peaks are in close agreement with the standard JCPDS No. 04-006-5378 of the crystal structure for cubic Ag_2O [42]. Furthermore, for Fe_2O_3, peaks were observed at 54.06° (116) and 62.38° (214), which are well matched with the JCPDS No. 00-001-1053 of the rhombohedral phase of Fe_2O_3. The presence of Fe_2O_3 and Ag_2O peaks in the XRD pattern of Fe_2O_3-Ag_2O/TiO_2 nanocomposites further confirmed the successful formation of heterojunctions [43–45].

3.4.2. FTIR Analysis

The FTIR spectra of all samples in the frequency range of 500–4000 cm^{-1} are shown in Figure 4. All of the samples showed peaks around 3200–3400 cm^{-1} for the stretching vibration of O-H and 1600 cm^{-1} for the bending vibration of the adsorbed water molecules. Furthermore, the broadening of the peak positioned at ~3500 cm^{-1} corresponds to O-H stretching vibration, which resulted in the formation of a new -OH group, most likely as a Ti-OH surface group. The Ti-O stretching and Ti-O-Ti bridging stretching modes were responsible for the broad intense band in the 450–700 cm^{-1} range. The intensity of the nanocomposites of TiO_2 incorporated with Fe_2O_3 and Ag_2O was found to be lower than that of pure TiO_2. This decrease in the intensity might have been due to the decrease in

bond energy, which produced a more microstructure chemical bond [46]. Additionally, the smaller amount of composites used in the analysis could have resulted in the decrease in the intensity of the nanocomposites. It was observed from the FTIR spectra that many of the peaks of Fe_2O_3 and Ag_2O overlapped with those of TiO_2 due to the similar peak positions. The presence of Ag_2O and Fe_2O_3 in the nanocomposites could be observed by the band ranging from 453 to 556 cm^{-1}. The band at ~541cm^{-1} corresponded to the Fe-O stretching mode of Fe_2O_3, while the band at 45–525 cm^{-1} could be assigned to the Ag-O bond [47].

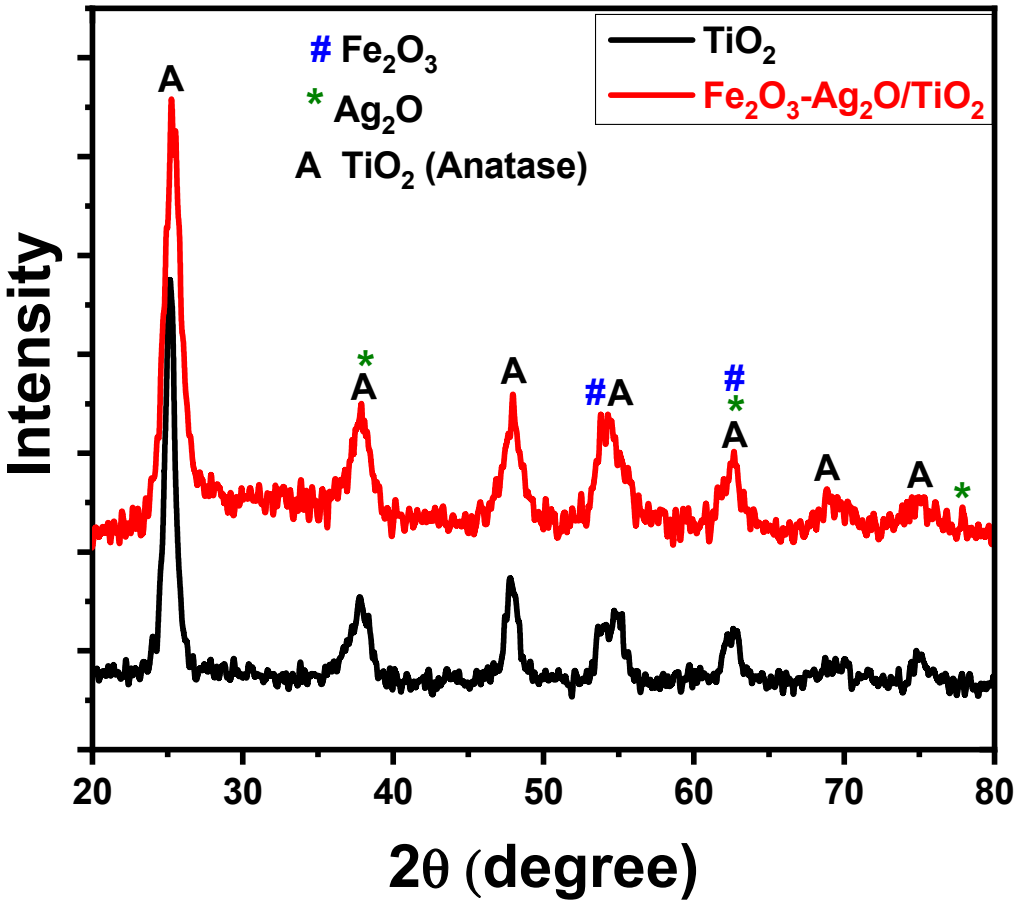

Figure 3. XRD patterns of pure TiO_2 and Fe_2O_3-Ag_2O/TiO_2 nanocatalyst.

3.5. Morphological Studies by Transmission Electron Microscopy

Transmission electron microscopy was used to examine the particle size, crystallinity, and morphology of the samples. Figure 5a depicts a TEM image of the nanocomposites containing Fe_2O_3-Ag_2O/TiO_2. The Fe_2O_3-Ag_2O/TiO_2 nanocatalyst was discovered to be almost entirely composed of tiny nanocrystallites. The inset of Figure 5a shows an HRTEM image of Fe_2O_3-Ag_2O/TiO_2 nanocatalyst. Here, an interplanar spacing d = 0.328 nm corresponding to Fe_2O_3 (110), d = 0.256 nm for TiO_2 (110) and d = 0.231 nm ascribed to the Ag_2O (100) phase can be seen, which revealed the existence of Fe_2O3 and Ag_2O in the TiO_2 nanocomposites with high crystallinity. The TEM image demonstrated that the individual nanoparticles produced were nearly spherical, and the calculated average particle size was found to be 50 nm with Image-J software (V 1.8.0) (see Figure 5b). To distinguish between Fe_2O_3, Ag_2O, and TiO_2, a small dot-like morphology was attributed to the Ag_2O nanoparticles, and these particles had uniform dispersion on the surface of TiO_2. However, the presence of Fe_2O_3 particles can be observed by two distinct colors in Figure 5a, in which darker-color particles (black) correspond to Fe_2O_3 or may be the agglomeration of TiO_2 nanoparticles, because some of the TiO_2 nanoparticles tended to aggregate. A TEM image of TiO_2 nanoparticles is shown in Figure 5c, where the spherical morphology of the

particles can be seen, with a particle size ranging from 60 to 65 nm. These nanoparticles tended to agglomerate, showing a chain-like morphology composed of spherical particles.

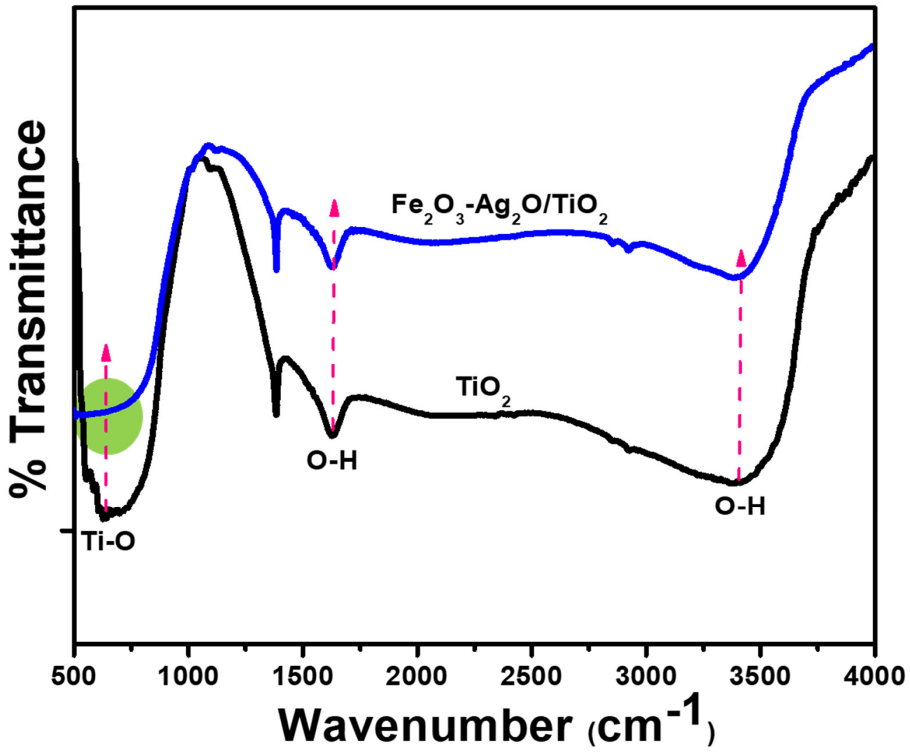

Figure 4. FTIR spectra of pure TiO_2 and Fe_2O_3-Ag_2O/TiO_2 nanocatalyst.

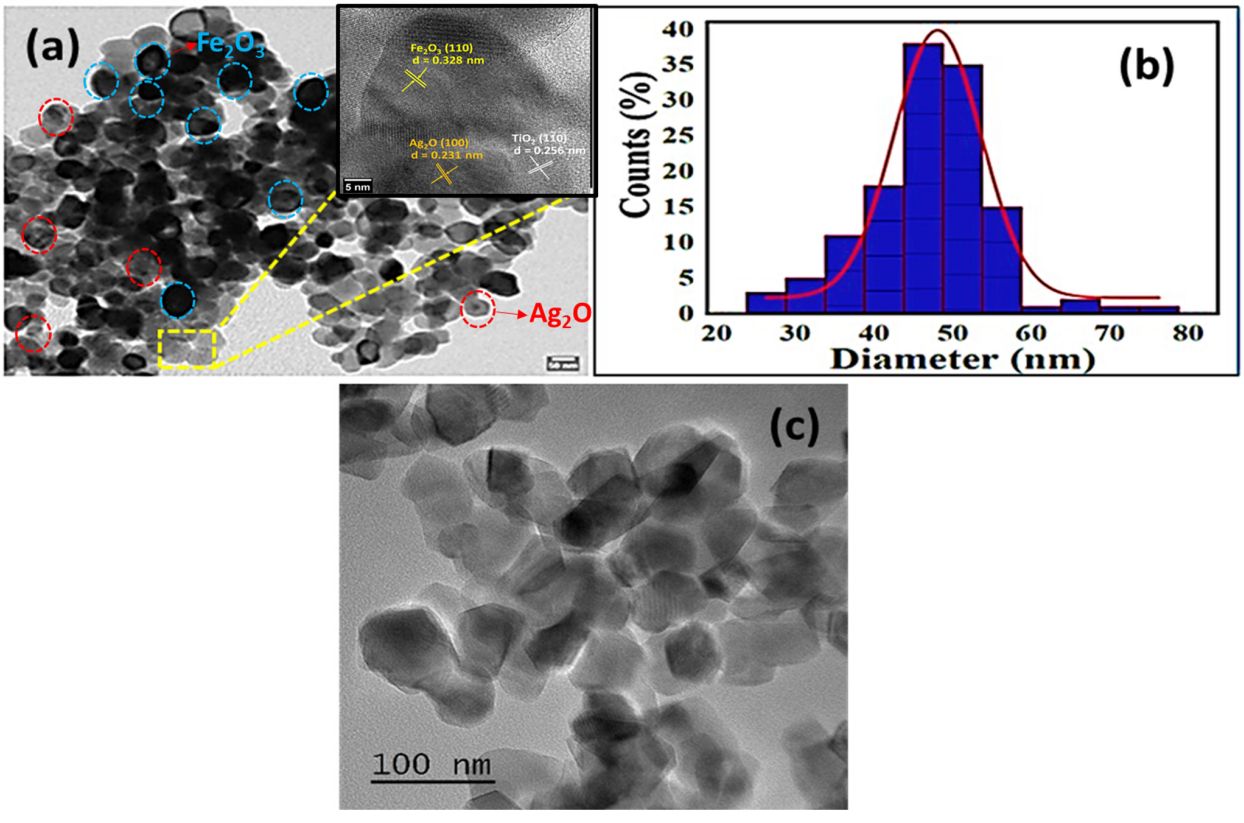

Figure 5. (**a**) TEM image of Fe_2O_3-Ag_2O/TiO_2 nanocatalyst, where inset shows the HRTEM image; (**b**) size distribution curve of Fe_2O_3-Ag_2O/TiO_2; (**c**) TEM image of TiO_2 nanocatalyst.

3.6. Energy Dispersive X-Ray (EDX) Spectra

The energy dispersive X-ray (EDX) spectrum of the Fe_2O_3- and Ag_2O-incorporated TiO_2 is shown in Figure 6. The peaks corresponding to Ti, O, and the incorporated metals of Fe and Ag can be confirmed in Figure 6. The results of the elemental analysis showed the successful incorporation of Fe_2O_3 and Ag_2O into the TiO_2 lattice.

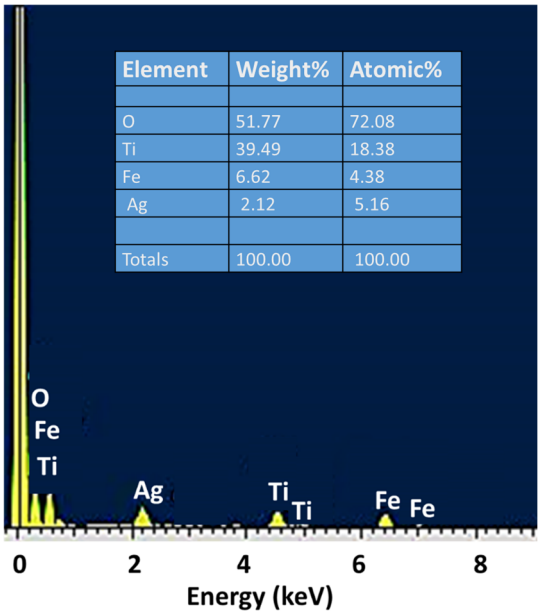

Figure 6. EDS spectrum of Fe_2O_3-Ag_2O/TiO_2 nanocatalyst.

3.7. Specific Surface Area

The specific surface area of the samples was determined by using the Brunauer–Emmet–Teller method. The BET specific surface area of TiO_2 was found to be 48.26 m^2/g; however, for the Fe_2O_3-Ag_2O/TiO_2 nanocatalyst, an increase in surface area of 56.18 m^2/g was observed. The increase in surface area of the nanocomposites might have been due to the incorporation of the small particles of Fe_2O_3 and Ag_2O compared with the large TiO_2 particles. It is well known that smaller size particles possess a larger surface area; therefore, the synergic effect of the incorporation of Fe_2O_3 and Ag_2O into TiO_2 resulted in an increase in the surface area of the nanocatalyst.

3.8. Effect of Catalyst Concentration

From the experimental results, we observed an acceleration in photocatalytic decontamination rate with the increase in concentration from 1 to 20 mg/L, whereas no increase in the rate was observed when the concentration of the Fe_2O_3-Ag_2O/TiO_2 was increased above 10 mg/L. The results for the effect of catalyst concentration are presented in Table 2.

Table 2. Effect of catalyst concentration on decontamination of Spiromesifen in media under direct sunlight.

Occasion (Hour)	Residues (mg/L)					
	0 mg/L Catalyst	1 mg/L Catalyst	5 mg/L Catalyst	10 mg/L Catalyst	15 mg/L Catalyst	20 mg/L Catalyst
8	0.987	0.831	0.625	0.423	0.426	0.429

3.9. Photocatalytic Studies

The Spiromesifen photocatalytic degradation results in alga and daphnia media revealed that the residues were unstable. Table S5 summarizes the results of the photocatalytic

studies, showing the kinetic parameters, rate constant (k), and DT50. Spiromesifen's half-life in alga and daphnia in the presence of a catalyst was 8.15 h and 7.41 h, respectively. The representative chromatograms are presented in Figure S2. Additionally, photocatalytic experiments in the alga and daphnia media using TiO_2, Fe_2O_3-TiO_2, and Ag_2O-TiO_2 were performed, and the results are presented in Table S6. Figure 7 shows the dissipation curves of the photocatalytic degradation of Spiromesifen in alga and daphnia media with TiO_2, Fe_2O_3-TiO_2, Ag_2O-TiO_2, and Fe_2O_3-Ag_2O/TiO_2 nanocomposites under direct sunlight. Figure 7a depicts the curve of degradation in the alga medium, and Figure 7b shows the curve in the daphnia medium. In both the curves, it can be observed that the degradation was faster in the beginning, but slowed as reaction time increased. It is clear from the curve in Figure 7a,b that the TiO_2 nanoparticles, Fe_2O_3/TiO_2, and Ag_2O/TiO_2 nanoparticles reached a minimum degradation value after 120 h, while for the nanocomposites of Fe_2O_3-Ag_2O/TiO_2, the minimum value was reached after only 48 h. By comparing the pure TiO_2 with the nanocomposites of TiO_2, it could be observed that with the incorporation of Fe_2O_3 and Ag_2O, the degradation was improved; the highest degradation rate was observed for Fe_2O_3-Ag_2O/TiO_2 nanocomposites. Furthermore, by comparing the media, Fe_2O_3-Ag_2O/TiO_2 nanocomposites showed better degradation efficiency in daphnia medium than in the alga medium. This improvement in the degradation efficiency could have been due to the increase in the surface are of nanocomposites achieved through the incorporation of Fe_2O_3 and Ag_2O, which provide more active sites for the dye, thereby increasing the rate of degradation [48,49]. Therefore, the prepared nanocomposites could be a photocatalyst suitable for the degradation of various contaminants.

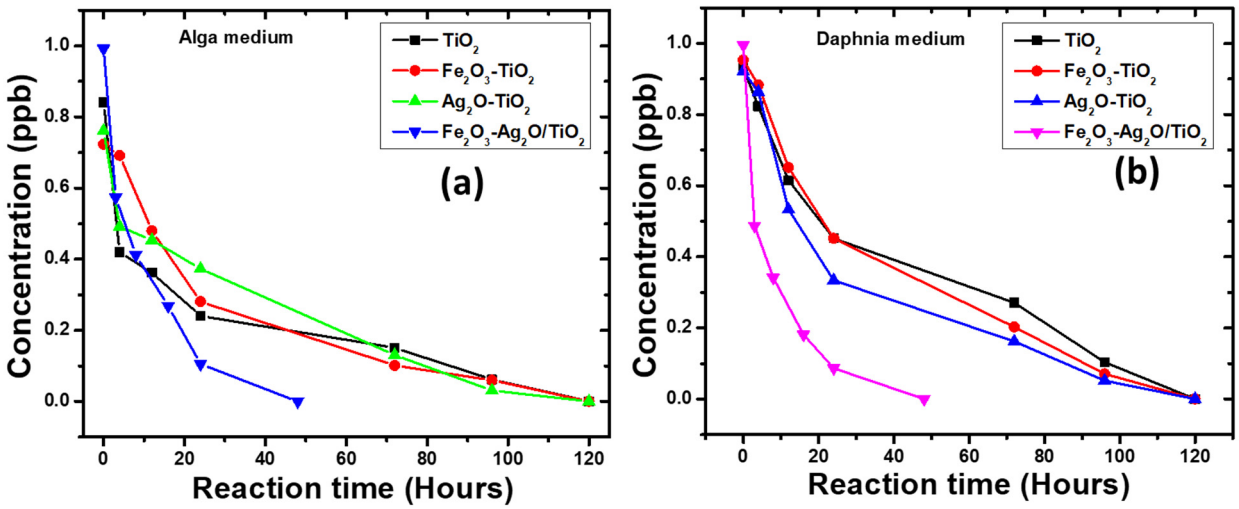

Figure 7. The dissipation curve of photocatalytic decontamination of Spiromesifen in alga (**a**) and daphnia (**b**) media under direct sunlight with TiO_2, Fe_2O_3-TiO_2, Ag_2O-TiO_2, and Fe_2O_3-Ag_2O/TiO_2 nanocomposites.

4. Conclusions

In summary, Fe_2O_3-Ag_2O/TiO_2 nanocomposites were prepared using the precipitation method and effectively demonstrated photocatalytic activity as nanocatalysts for the photocatalytic degradation of Spiromesifen when exposed to sunlight. XRD studies confirmed the single-phase nature of the nanocatalysts without any impurity or secondary phase formation. The results of morphological studies using SEM and TEM showed that the nanoparticles were spherical with a size ranging from 15 to 60 nm. The photocatalysis of Spiromesifen using Fe_2O_3-Ag_2O/TiO_2 nanocatalysts was carried out in two media under direct sunlight. The optimum catalyst concentration was 10 mg/L, and the results showed that the half-life of Spirodiclofen pesticide was ~10 days without the nanocatalysts, however, with the nanocatalysts, the half-life of Spirodiclofen was ~8 h at most. Furthermore, the Spirodiclofen residues in different aquatic toxic media were determined by using a

simple sensitive validated LC-MS/MS analytical method. These results depicted that Fe_2O_3-Ag_2O/TiO_2 nanocatalysts could be candidates for the degradation of toxic elements in the near future.

Supplementary Materials: The following supporting information can be downloaded at: https://www.mdpi.com/article/10.3390/cryst13040644/s1, Figure S1: SEM images of Fe2O3-Ag2O/TiO2 nanocatalyst; Figure S2: Representative Photocatalytic 0th-hour Spiromesifen standard (a), alga (b) and daphnia (c) samples LC-MS/MS MRM Chromatograms; Table S1: Composition of the alga (OECD TG 201) Medium; Table S2: Daphnia magna (M4 Medium) Netrunts; Table S3: Recovery and repeatability in Alga Medium; Table S4: Recovery and repeatability in Daphnia magna Medium; Table S5: Kinetic parameters for photocatalytic decontamination of Spiromesifen in Alga and Daphnia under direct sunlight using Fe2O3-Ag2O-TiO2 nanocomposites; Table S6: Kinetic parameters for photocatalytic decontamination of Spiromesifen in Alga and Daphnia under direct sunlight using TiO2, Fe2O3-TiO2 and Ag2O-TiO_2 nanocomposites.

Author Contributions: Conceptualization, F.A.; data curation, F.A., T.N.R., N.A. and Y.P.; formal analysis, F.A., T.N.R. and Y.P.; funding acquisition, F.A.; investigation, N.A.; Methodology, F.A. and T.N.R.; resources, S.K. and A.A.; software, S.K.; supervision, A.A.; validation, N.A. and A.A.; visualization, T.N.R.; writing—original draft, F.A. and T.N.R.; writing—review and editing, F.A., T.N.R., N.A., Y.P., S.K. and A.A. All authors have read and agreed to the published version of the manuscript.

Funding: This work was supported by the Deputyship for Research and Innovation, Ministry of Education in Saudi Arabia, Project number INST091.

Institutional Review Board Statement: Not applicable.

Informed Consent Statement: Not applicable.

Data Availability Statement: Data are available upon reasonable request.

Acknowledgments: The authors extend their appreciation to the Deputyship for Research and Innovation, Ministry of Education in Saudi Arabia for funding this research work through the project number INST091.

Conflicts of Interest: The authors declare no conflict of interest.

References

1. Escher, B.I.; Bramaz, N.; Mueller, J.F.; Quayle, P.; Rutishauser, S.; Vermeirssen, E.L.M. Toxic Equivalent Concentrations (TEQs) for Baseline Toxicity and Specific Modes of Action as a Tool to Improve Interpretation of Ecotoxicity Testing of Environmental Samples. *J. Environ. Monit.* **2008**, *10*, 612–621. [CrossRef]
2. Berrebaan, I.; Montassir, L.; Saadallah, M.; Bouchtaoui, S.; Bessi, H. Applicability of Miniscale Algal Growth Inhibition Bioassay Using Microtitration in the Central Moroccan Laboratory (ONEE). *J. Mater. Environ. Sci.* **2018**, *2508*, 1306–1311.
3. Chen, C.Y.; Wang, Y.J.; Yang, C.F. Estimating Low-Toxic-Effect Concentrations in Closed-System Algal Toxicity Tests. *Ecotoxicol. Environ. Saf.* **2009**, *72*, 1514–1522. [CrossRef]
4. Yamagishi, T.; Yamaguchi, H.; Suzuki, S.; Horie, Y.; Tatarazako, N. Cell Reproductive Patterns in the Green Alga *Pseudokirchneriella subcapitata* (=*Selenastrum capricornutum*) and Their Variations under Exposure to the Typical Toxicants Potassium Dichromate and 3,5-DCP. *PLoS ONE* **2017**, *12*, e0171259. [CrossRef]
5. Rottmann, R.W. *Culture Techniques of Moina: Ideal Daphnia for Feeding Freshwater Fish Fry*; Florida Cooperative Extension Service, Institute of Food and Agricultural Sciences, University of Florida: Gainesville, FL, USA, 1992; pp. 1–6.
6. Munirasu, S.; Uthayakumar, V.; Arunkumar, P.; Ramasubramanian, V. 4-2-91-301. *Int. J. Fish. Aquat. Stud.* **2016**, *4*, 5–10.
7. Tato, T.; Beiras, R. The Use of the Marine Microalga Tisochrysis Lutea (T-Iso) in Standard Toxicity Tests; Comparative Sensitivity with Other Test Species. *Front. Mar. Sci.* **2019**, *6*, 488. [CrossRef]
8. Pleiter, M.G. Individual and Mixture Toxicity of Pharmaceuticals towards Microalgae. Role of Intracellular Free Ca^{2+}. Ph.D. Thesis, Universidad Autónoma de Madrid, Madrid, Spain, 2017.
9. Katsumata, M.; Koike, T.; Nishikawa, M.; Kazumura, K.; Tsuchiya, H. Rapid Ecotoxicological Bioassay Using Delayed Fluorescence in the Green Alga Pseudokirchneriella Subcapitata. *Water Res.* **2006**, *40*, 3393–3400. [CrossRef]
10. Schade, S.; Butler, E.; Gutsell, S.; Hodges, G.; Colbourne, J.K.; Viant, M.R. Improved Algal Toxicity Test System for Robust Omics-Driven Mode-of-Action Discovery in Chlamydomonas Reinhardtii. *Metabolites* **2019**, *9*, 94. [CrossRef]
11. Rodiana, Y.; Settachan, D.; Saneanukul, T.; Diamond, J. Comparison Between Acute Toxicity and Chemical Analysis of Natural Gas Drilling Effluent Samples Using Penaeus Monodon. *J. Ecolab* **2011**, *5*, 45–54. [CrossRef]

12. Stanley, A.S.; Rajaretnamand, S. Studies on the Toxicological Effects of Bimetals on the Cladoceran, Daphnia Magna and Examination of Histopathological Effects through Transmission Electron Microscopy (TEM). *J. Chem. Pharm. Res.* **2015**, *7*, 506–511.
13. Chang, F.; Yi, M.; Li, H.; Wang, J.; Zhao, X.; Hu, X.; Qi, Q. Antibiotic Toxicity Isolated and as Binary Mixture to Freshwater Algae Raphidocelis Subcapitata: Growth Inhibition, Prediction Model, and Environmental Risk Assessment. *Toxics* **2022**, *10*, 739. [CrossRef] [PubMed]
14. Kiljanek, T.; Niewiadowska, A.; Małysiak, M.; Posyniak, A. Miniaturized Multiresidue Method for Determination of 267 Pesticides, Their Metabolites and Polychlorinated Biphenyls in Low Mass Beebread Samples by Liquid and Gas Chromatography Coupled with Tandem Mass Spectrometry. *Talanta* **2021**, *235*, 122721. [CrossRef] [PubMed]
15. Nam, Y.S.; Her, J.Y.; Hwang, J.; Lee, K.G. Pesticide Residues in Yuza (Citrus Junos) Cultivated Using Ordinary and Environmentally Friendly Cultures. *J. Pestic. Sci.* **2015**, *40*, 60–64. [CrossRef]
16. Hollosi, L.; Mittendorf, K. *Determination of Pesticides in Grapes, Baby Food and Wheat Flour by Automated Online Sample Preparation LC-MS/MS*; Thermo Fisher Scientific Inc.: Waltham, MA, USA, 2005.
17. El-Gammal, H.A.; Ibrahim, E.D.S.; Ahmed, M.M. Field Efficacy of Acaricides on Citrus Red Mite and Dissipation Study for Cyflumetofen and Pyridaben in Lemon Fruit Using QuEChERS Method and LC-ESI-MS/MS. *Egypt. J. Chem.* **2022**, *65*, 139–146. [CrossRef]
18. Eriksson, E. Pesticide Screening Method with UPLC-MS/MS. *Calibration Valid. Anal. Methods A Sampl. Curr. Approaches* **2015**, 40.
19. Zhang, J.; Li, M.; Li, Y.; Li, Z.; Wang, F.; Li, Q.; Zhou, W.; Lu, R.; Gao, H. Application of Ionic-Liquid-Supported Magnetic Dispersive Solid-Phase Microextraction for the Determination of Acaricides in Fruit Juice Samples. *J. Sep. Sci.* **2013**, *36*, 3249–3255. [CrossRef]
20. Pohorecka, K.; Szczęsna, T.; Witek, M.; Miszczak, A.; Sikorski, P. The Exposure of Honey Bees to Pesticide Residues in the Hive Environment about Winter Colony Losses. *J. Apic. Sci.* **2017**, *61*, 105–125. [CrossRef]
21. Ge, X.; Wu, X.; Qi, H.; Qin, X.; Sun, H. A Simple and Effective Method for the Determination of Chlorantraniliprole and Spirodiclofen in Tobacco by Liquid Chromatography after Accelerated Solvent Extraction and Silica Gel Clean-Up. *J. Liq. Chromatogr. Relat. Technol.* **2014**, *37*, 145–154. [CrossRef]
22. Almeida, M.O.; Oloris, S.C.S.; Faria, V.H.F.; Ribeiro, M.C.M.; Cantini, D.M.; Soto-Blanco, B. Optimization of Method for Pesticide Detection in Honey by Using Liquid and Gas Chromatography Coupled with Mass Spectrometric Detection. *Foods* **2020**, *9*, 1368. [CrossRef]
23. Shin, Y.; Kim, C.J.; Baek, S.; Kim, L.; Son, K.A.; Lee, H.D.; Kim, D.; Kim, J.H.; Noh, H.H. Liquid Chromatography-Tandem Mass Spectrometry for the Simultaneous Analysis of 353 Pesticides in the Edible Insect Tenebrio Molitor Larvae (Mealworms). *Molecules* **2020**, *25*, 5866. [CrossRef]
24. Bellisai, G.; Bernasconi, G.; Brancato, A.; Carrasco Cabrera, L.; Ferreira, L.; Giner, G.; Greco, L.; Jarrah, S.; Kazocina, A.; Leuschner, R.; et al. Review of the Existing Maximum Residue Levels for Spirodiclofen According to Article 12 of Regulation (EC) No 396/2005. *EFSA J.* **2021**, *19*, e06908. [CrossRef]
25. Al-rimawi, F. A Hplc-Uv Method for Determination of a Hplc-Uv Method for Deteermination of Three Pesticides. *Int. J. Adv. Chem.* **2014**, *2*, 1–8.
26. Tian, F.; Qiao, C.; Wang, C.; Luo, J.; Guo, L.; Pang, T.; Li, J.; Wang, R.; Pang, R.; Xie, H. Simultaneous Determination of Spirodiclofen, Spiromesifen, and Spirotetramat and Their Relevant Metabolites in Edible Fungi Using Ultra-Performance Liquid Chromatography/Tandem Mass Spectrometry. *Sci. Rep.* **2021**, *11*, 1547. [CrossRef]
27. Sun, H.; Liu, C.; Wang, S.; Liu, Y.; Liu, M. Dissipation, Residues, and Risk Assessment of Spirodiclofen in Citrus. *Environ. Monit. Assess.* **2013**, *185*, 10473–10477. [CrossRef]
28. El-Saeid, M.H.; Baqais, A.; Alshabanat, M. Study of the Photocatalytic Degradation of Highly Abundant Pesticides in Agricultural Soils. *Molecules* **2022**, *27*, 634. [CrossRef] [PubMed]
29. Sahithya, K.; Das, N. Remediation of Pesticides Using Nanomaterials: An Overview. *Int. J. ChemTech Res.* **2015**, *8*, 86–91.
30. Morsy, A.R.; El-Hefny, D.E. Residues Assessment of Captan, Spirodiclofen and Thiophanate Methyl in Apple Fruits under the Field Conditions. *Middle East J. Agric. Res.* **2017**, *6*, 135–142.
31. Sarteep, Z.; Pirbazari, A.E.; Aroon, M.A. Silver Doped TiO_2 Nanoparticles: Preparation, Characterization and Efficient Degradation of 2,4-Dichlorophenol Under Visible Light. *Nanotechnol. J. Water Environ. Nanotechnol.* **2016**, *1*, 135–144. [CrossRef]
32. Sun, Y.; O'Connell, D.W. Application of Visible Light Active Photocatalysis for Water Contaminants: A Review. *Water Environ. Res.* **2022**, *94*, e10781. [CrossRef]
33. Gómez-Pastora, J.; Dominguez, S.; Bringas, E.; Rivero, M.J.; Ortiz, I.; Dionysiou, D.D. Review and perspectives on the use of magnetic nano photocatalysts (MNPCs) in water treatment. *Chem. Eng. J.* **2017**, *310*, 407–427. [CrossRef]
34. Chen, F. Synergistic effect of CeO_2 modified TiO_2 photocatalyst on the enhancement of visible light photocatalytic performance. *J. Alloys Compd.* **2017**, *714*, 560–566. [CrossRef]
35. Gao, Q.; Wu, X.; Fan, Y. Dyes and Pigments the efect of iron ions on the anatase erutile phase transformation of titania (TiO_2) in mica titania pigments. *Dye. Pigment.* **2012**, *95*, 96–101. [CrossRef]
36. Liu, H.; Shon, H.K.; Sun, X.; Vigneswaran, S.; Nan, H. Preparation and characterization of visible light responsive Fe_2O_3–TiO_2 composites. *Appl. Surf. Sci.* **2011**, *257*, 5813–5819. [CrossRef]
37. Wang, T. Orthogonal synthesis, structural characteristics and enhanced visible-light photocatalysis of mesoporous Fe_2O_3/TiO_2 hetero structured microspheres. *Appl. Surf. Sci.* **2014**, *311*, 314–323. [CrossRef]

38. Ghorai, T.K.; Chakraborty, M.; Pramanik, P. Photocatalytic performance of nano-photocatalyst from TiO_2 and Fe_2O_3 by mechanochemical synthesis. *J. Alloys Compd.* **2011**, *509*, 8158–8164. [CrossRef]
39. Li, R.; Jia, Y.; Bu, N.; Wu, J.; Zhen, Q. Photocatalytic degradation of methyl blue using Fe_2O_3/TiO_2 composite ceramics. *J. Alloys Compd.* **2015**, *643*, 88–93. [CrossRef]
40. Tu, Y.; Huang, S.; Sang, J.; Zou, X. Preparation of Fe-doped TiO_2 nanotube arrays and their photocatalytic activities under visible light. *Mater. Res. Bull.* **2010**, *45*, 224–229. [CrossRef]
41. Wei, N.; Cui, H.Z.; Song, Q.; Zhang, L.Q.; Song, X.J.; Wang, K.; Zhang, Y.F.; Li, J.; Wen, J.; Tian, J. Ag_2O nanoparticle/TiO_2 nanobelt heterostructures with remarkable photo-response and photocatalytic properties under UV, visible and near-infrared irradiation. *Appl. Catal. B* **2016**, *198*, 83. [CrossRef]
42. Ren, H.T.; Yang, Q. Fabrication of Ag_2O/TiO_2 with enhanced photocatalytic performances for dye pollutants degradation by a pH-induced method. *Appl. Surf. Sci.* **2017**, *396*, 530–538. [CrossRef]
43. Widyaningtyas, A.L.; Yulizar, Y.; Apriandanu, D.O.B. Ag_2O nanoparticles fabrication by Vernonia amygdalina Del. leaf extract: Synthesis, characterization, and its photocatalytic activities. *IOP Conf. Ser. Mater. Sci. Eng.* **2019**, *509*, 012022. [CrossRef]
44. Wenjuan, L.; Liang, R.; Hu, A.; Huang, Z.; Zhou, Y.N. Generation of oxygen vacancies in visible light activated one-dimensional iodine TiO_2 photocatalysts. *RSC Adv.* **2014**, *4*, 36959–36966.
45. Xia, L.Y.Y. Core-Shell Structured α-Fe_2O_3@TiO_2 Nanocomposites with Improved Photocatalytic Activity in Visible Light Region. *Phys. Chem. Chem. Phys.* **2013**, *15*, 18627–18634. [CrossRef] [PubMed]
46. Mahadik, M.A. Visible light catalysis of rhodamine B using nanostructured Fe_2O_3, TiO_2 and TiO_2/Fe_2O_3 thin flms. *J. Photochem. Photobiol. B Biol.* **2014**, *133*, 90–98. [CrossRef]
47. Mohamed, M.A.; Jaafar, J.; Ismail, A.F.; Othman MH, D.; Rahman, M.A. Chapter 1—Fourier Transform Infrared (FTIR) Spectroscopy. In *Membrane Characterization*; Hilal, N., Ismail, A.F., Matsuura, T., Oatley-Radcliffe, D., Eds.; Elsevier: Amsterdam, The Netherlands, 2017; pp. 3–29.
48. Ma, S.; Xue, J.; Zhou, Y.; Zhang, Z. Enhanced visible-light photocatalytic activity of Ag_2O/gC_3N_4 p–n heterojunctions synthesized via a photochemical route for degradation of tetracycline hydrochloride. *RSC Adv.* **2015**, *27*, 3708–3715.
49. Chen, V.; Ma, P. The effect of surface area on the degradation rate of nano-fibrous poly(l-lactic acid) foams. *Biomaterials* **2006**, *27*, 3708–3715. [CrossRef]